



Tuning the morphology of electrospayed BiVO_4 from nanopillars to nanoferns via pH control for solar water splitting



Min-Woo Kim ^{a,1}, Edmund Samuel ^{a,1}, Karam Kim ^a, Hyun Yoon ^b, Bhavana Joshi ^a, Mark T. Swihart ^c, Sam S. Yoon ^{a,*}

^a School of Mechanical Engineering, Korea University, Seoul, 02841, Republic of Korea

^b KIER-UNIST Advanced Center for Energy, Korea Institute of Energy Research (KIER), 50, UNIST-gil, Ulsan, 44919, Republic of Korea

^c Department of Chemical & Biological Engineering, University at Buffalo, The State University of New York, Buffalo, NY, 14260-4200, USA

ARTICLE INFO

Article history:

Received 26 March 2018

Received in revised form

12 July 2018

Accepted 14 July 2018

Available online 20 July 2018

Keywords:

Electrostatic spray deposition

BiVO_4

Nanopillar

Nanofern

Solar water splitting

Photocurrent density

ABSTRACT

Electrospayed BiVO_4 adopts a nanopillar structure formed by diffusion-limited aggregation, which maximizes the surface area of the nanopillars. However, increasing the interfacial area between an electrode and the electrolyte through nanostructuring enhances the overall interfacial activity for solar water splitting. For this purpose, the pH of the precursor solution used for electrospaying BiVO_4 was altered by adding ammonium hydroxide, thereby inducing a drastic change in the morphology of BiVO_4 . The previously demonstrated nanopillar morphology of electrospayed BiVO_4 was transformed into a nanofern structure that increased the photocurrent density of BiVO_4 from 0.82 to 1.23 $\text{mA} \cdot \text{cm}^{-2}$ at 1.2 V vs. Ag/AgCl. The produced films were characterized by scanning electron microscopy, X-ray photoelectron spectroscopy, Raman spectroscopy, and electrochemical impedance spectroscopy.

© 2018 Elsevier B.V. All rights reserved.

1. Introduction

Fujishima and Honda pioneered photoelectrochemical (PEC) water splitting as a method to generate renewable energy by converting sunlight into stored chemical energy in the form of hydrogen [1]. Since then, research on the PEC water splitting process has mushroomed [2]. In a typical PEC process, hydrogen is produced at the photocathode, while oxygen is produced at the photoanode. Thus, the electrochemical properties of photoelectrodes, such as their bandgap, band alignment, photovoltage, electron–hole separation, and charge carrier mobility, are important design factors to consider, to achieve the most efficient PEC electrodes [3].

Many different metal oxides have been studied for use as the photoanode for water splitting, including TiO_2 , Fe_2O_3 , WO_3 , and BiVO_4 [4–11]. To improve the PEC performance of these metal oxides, Hejazi et al. reported aminated TiO_2 nanotubes of TiO_2 [5], Liu et al. controlled the morphology of $\alpha\text{-Fe}_2\text{O}_3$ using additives [7], and Wang et al. utilized the conducting polymer polyaniline for hole

transport along with BiVO_4 [11]. Among these oxides, BiVO_4 , with a bandgap of 2.4–2.6 eV, is a good candidate as a photoanode material because it can absorb visible light. BiVO_4 is relatively non-toxic and contains mainly earth-abundant elements, which supports its potential as a cost-effective and commercially viable anode material. However, short carrier diffusion length and relatively fast charge recombination due to low electron mobility in BiVO_4 are its main shortcomings, which prevent it from achieving its maximum theoretical photocurrent density of 7.5 $\text{mA} \cdot \text{cm}^{-2}$.

Elemental doping is an effective way to minimize the recombination of photogenerated electron–hole pairs. Multilayer heterostructures have been introduced as a means of increasing light absorption [12–17]. Alternatively, varying the physical morphology of monoclinic scheelite BiVO_4 (m- BiVO_4) has been attempted and has been proven to effectively enhance the photocatalytic activity of BiVO_4 [18–20].

Sol-gel, microwave-assisted, co-precipitation, solution combustion, and hydrothermal approaches have been used for the deposition of m- BiVO_4 on various substrates, where the morphology of the oxide differs depending on the deposition method [21–23]. Lu et al. fabricated m- BiVO_4 with diverse morphologies by employing various organic additives such as polyethylene glycol, sodium

* Corresponding author.

E-mail address: skyoona@korea.ac.kr (S.S. Yoon).

¹ These authors have contributed equally.

dodecyl benzene sulfonate, and urea [21]. Interesting nanostructures of BiVO_4 in the form of spheres, peanuts, dumbbells, flowers, sheets, nanotubes, leaves, and octopods have also been fabricated by varying the pH of the solvent during the hydrothermal reaction [24,25]. Moreover, the effects of the pH on the morphology and the preferential (040) orientation of BiVO_4 were illustrated by Chen et al. [26], who used a solvothermal process. In our earlier study, we demonstrated the electro-spray deposition (ESD) of BiVO_4 with a pillar structure and improved PEC performance [10,27]. However, the effects of altering the pH of the electro-spraying solution on the morphology of BiVO_4 , and consequently the photocurrent density of the PEC water splitting process, have never been reported. Varying the pH of the ESD precursor solution enabled us to change the pillar structures to more open fern-like structures that can provide a better combination of incident light absorption and charge-carrier transport to the electrode–electrolyte interface, thereby improving the PEC performance.

Here, for the first time, we demonstrate the effect of the pH of the ESD precursor solution on the morphology of deposited BiVO_4 films and the photocurrent density achieved with these films as photoanodes. We previously demonstrated the fabrication of BiVO_4 nanopillars using ESD [10]; however, the morphological changes induced by adjusting the pH of the reaction medium have not been studied. The features and advantages of the non-vacuum ESD technique have been discussed in earlier reports [17,28–32]. In this study, we explore the effect of varying the precursor solution pH on the morphology of BiVO_4 , and identify optimal conditions that maximize PCD. The pH of the BiVO_4 precursor solution was increased by adding ammonium hydroxide (AH). The ESD precursor solution with higher pH produced films with a nanofern, rather than nanopillar, morphology, which affected the PEC performance through changes in the surface area, light absorbance, and charge carrier transport properties of the nanostructures.

2. Experimental procedures

2.1. Deposition of *m*- BiVO_4 photoanodes

Fig. 1 shows the process used to prepare the precursor solution to fabricate the pH-controlled BiVO_4 films. The precursor solution

was prepared by mixing 1.08 g of bismuth(III) nitrate pentahydrate ($\text{BiN}_3\text{O}_9 \cdot 5\text{H}_2\text{O}$, $\geq 98\%$, Sigma-Aldrich) and 0.78 g of vanadium(III) acetylacetonate ($\text{V}(\text{C}_5\text{H}_7\text{O}_2)_3$, Sigma-Aldrich) in 10 mL of acetic acid (CH_3COOH , 99.7%, Samchun Chemicals) at room temperature (25 °C). Different amounts of an ACS-reagent-grade AH solution (28.0–30.0% NH_4OH , Sigma-Aldrich) were added to the BiVO_4 precursor solution to control the morphology of the BiVO_4 product. The use of 0, 1, 1.5, and 2 mL of AH resulted in final pH values of approximately 0, 4, 6, and 8 respectively; in the absence of AH, the pH of the solution was 0 as acetic acid was used as the solvent. Based on the volume of AH added to the precursor, the resultant BiVO_4 films are denoted as **BVO-0**, **BVO-1**, **BVO-1.5**, and **BVO-2**. The added amount of AH was restricted to 2 mL because exceeding this amount led to poor adhesion of deposited films when they were placed in the electrolyte for PEC testing.

Precursor solutions with different concentrations of NH_4OH were deposited on an indium tin oxide (ITO)-coated glass substrate by the electrostatic spray technique over the course of 60 min at a flow rate of $30 \mu\text{L h}^{-1}$. A high voltage (10.5 kV) was applied to the nozzle to ensure a stable Taylor cone. The substrate temperature was maintained at 80 °C. Finally, the films were annealed at 550 °C for 10 min. The schematic illustration in Fig. 1 depicts the solution preparation (Fig. 1a) technique, variation in the pH upon adding AH (Fig. 1b), and the ESD setup (Fig. 1c). Adding AH significantly transforms the morphology of BiVO_4 , as shown in Fig. 1d.

2.2. Characterization of pH-controlled BiVO_4

X-ray diffraction (XRD, Rigaku, Japan, D/max-2500) was performed with $\text{Cu-K}\alpha$ radiation over the 2θ range of 20–60° to analyze the structure of the BiVO_4 films. The Raman spectrum of the films was studied by using a Raman spectrometer (LabRam ARAMIS IR2, Horiba Jobin Yvon). The morphology of the BiVO_4 films was characterized using high-resolution scanning electron microscopy (HR-SEM, XL30 SFEI, Phillips Co., Holland) at 15 kV and high-resolution transmission electron microscopy (HR-TEM, JEM 2100F, JEOL Inc.). The PEC performance of the various BiVO_4 films was measured by water splitting tests based on PCD measurements. Each deposited BiVO_4 film was individually used as the working electrode, while an Ag/AgCl electrode and a piece of platinum wire

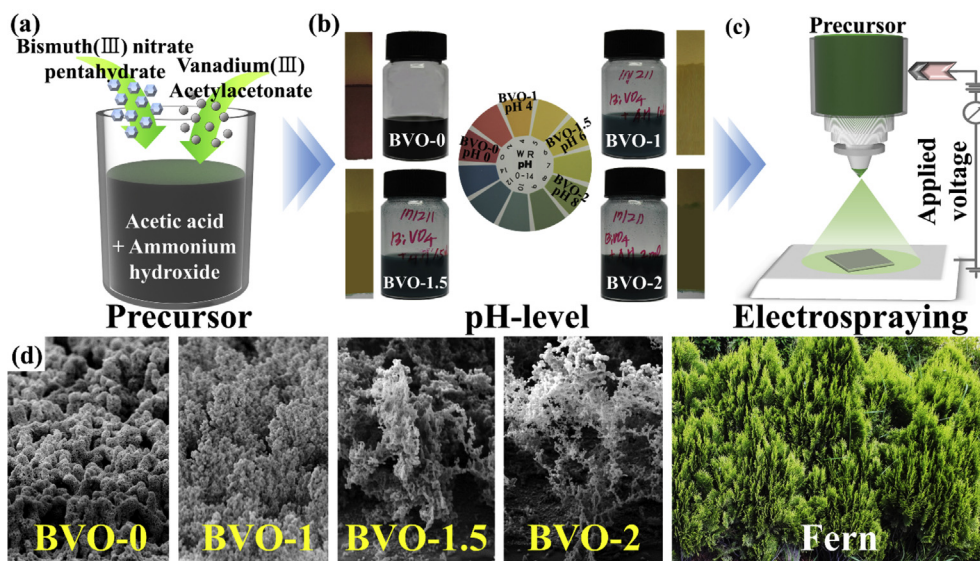


Fig. 1. Schematic illustration of the deposition of the BiVO_4 photoanode: (a) preparation of the precursor, (b) precursor solutions with different pH, (c) electro-spray deposition and (d) SEM images illustrating the morphological transformation corresponding to synthesis pH.

were employed as the reference and counter electrodes, respectively. The PEC measurements were performed in 0.5 M Na₂SO₄ (pH 7) as the electrolyte. A Xe arc lamp (Newport, Oriel Instruments, USA) equipped with an AM 1.5 filter was used to simulate sunlight. The PCD was measured using a potentiostat (VersaSTAT-3, Princeton Applied Research, USA) in the applied voltage range from -0.4 – 1.2 V (vs. Ag/AgCl); the scan rate used for the measurements was 10 mV s^{-1} . Further, electrochemical impedance spectroscopy (EIS) measurements were performed using the potentiostat described above and the same electrode configuration. The Bode phase plots were measured at 0.4 V (versus Ag/AgCl); a small sinusoidal perturbation (amplitude of 10 mV) was applied to the potential [14] over a frequency range of 100 kHz to 100 mHz under dark and illuminated conditions. The measured spectra were fitted using the ZSimpWin program (VersaStudio).

3. Results and discussion

3.1. Film characterization

The impact of adding various amounts of AH is evident from the SEM images presented in Fig. 2. For better visualization, the SEM images were acquired at an angle of about 70° . Fig. 2a shows the pillar-shaped BiVO₄ formed in the absence of AH (BVO-0), which is consistent with our previous study [10]. These BiVO₄ pillars (height $\sim 3 \mu\text{m}$) comprise particles of 200 – 250 nm in size arranged in a pillar shape; the particles were uniformly deposited over the ITO substrate. However, adding AH dramatically changed the morphology, as indicated in Fig. 2b–d. When 1 mL of AH was added, the BiVO₄ particles were ejected from the cone-jet and deposited to a thickness of about $5 \mu\text{m}$ on the ITO substrate, forming a branched fern morphology. The morphological change of BiVO₄ from pillar to branched is due to changing the properties of the precursor solution, which causes faster nucleation and slower crystal growth [33,34]. The precursor solution with higher pH results in a larger number of smaller crystal nuclei, simultaneously consuming protons due to the lower crystal growth rate [35]. Thus, the increased pH decreases the amount of free Bi³⁺ in the precursor

solution, which significantly affects the morphology of BiVO₄ after recrystallization during heat treatment in air at 500°C [36]. Moreover, electrostatic repulsion between these particles resulted in a branched structure. Fig. 2c and d shows the SEM images of BVO-1.5 and BVO-2.0, respectively. Fig. 2c shows that the particles formed branched fern and nanofern-like shapes (Fig. 2d) because the particles were better dispersed. Moreover, the thickness of the BiVO₄ layer on the ITO substrate increased with increasing concentrations of AH.

Thus, the SEM images confirm that varying the pH by adding AH significantly influences the morphology of BiVO₄. Increasing the AH concentration escalates the thermodynamic driving force for BiVO₄ precipitation [33], resulting in a faster nucleation rate. Furthermore, the BiVO₄ particles self-assemble into a specific morphology due to highly oriented colloidal aggregation of the nanoparticles at the precursor solution droplet/air interface [37]. More BiVO₄ particles deposit at the tips of the growing fern-like structures due to the electrostatic attraction between the deposited and incoming particles. These dynamics produce a less dense fern-like morphology rather than the nanopillar morphology formed in the absence of AH [38]. The effect of morphology on absorbance and light scattering is evident from the UV visible extinction spectra shown in Fig. S1. The extinction slightly decreased as the pH increased from 0 to 8. This trend may be due to decreased film density, which decreases the effective refractive index of the film, as well as decreased scattering due to the decreasing particle size with increasing pH. Thus, the lower apparent absorbance in these extinction measurements may not actually correspond to less absorbance by the films; rather, it may simply be less scattering [39].

Further, the impact of varying pH on the oxidation state of the elements in the BiVO₄ films was studied. Fig. 3a shows the survey spectra of BVO-0 and BVO-2. Both spectra show binding energy peaks related to Bi4f, V2p, and O1s. The core element spectrum of Bi4f (Fig. 3b) shows peaks at 163.5 and 158.3 eV, attributed to Bi4f_{5/2} and Bi4f_{7/2}, respectively, indicating the presence of Bi³⁺ in the samples. These binding energies are typical of the Bi4f state in BiVO₄ [40–42]. The V2p core spectra in Fig. 3c display peaks

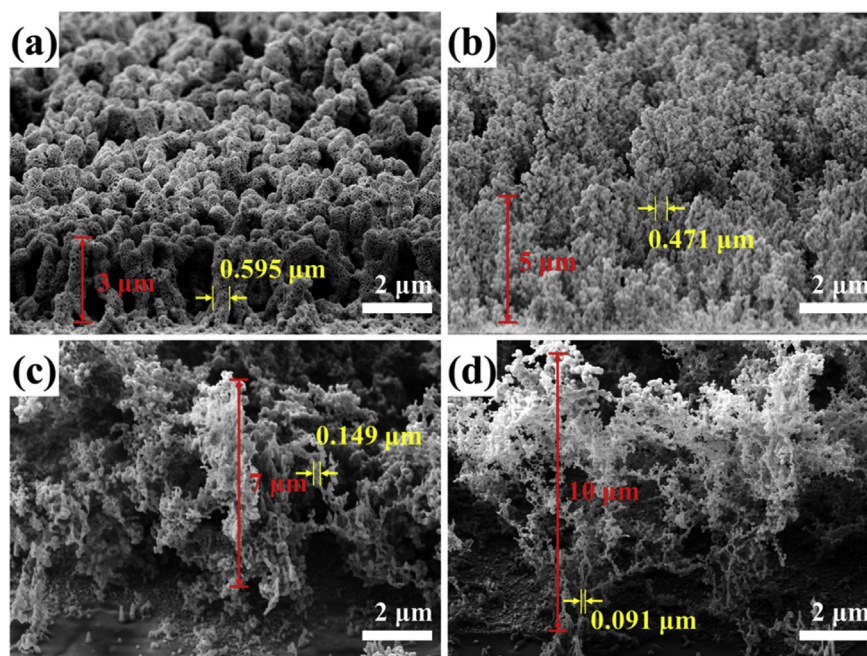


Fig. 2. SEM images illustrating the transformation of BiVO₄ from a nanopillar to a nanofern morphology: (a) BVO-0, (b) BVO-1, (c) BVO-1.5, and (d) BVO-2.

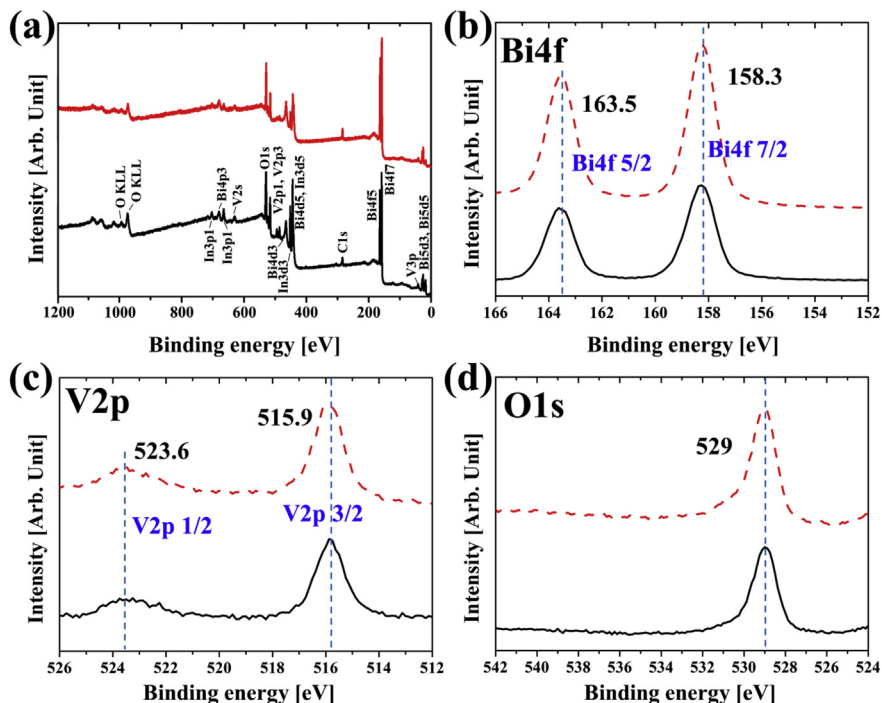


Fig. 3. XPS spectra: survey (a) and core spectra of (b) Bi4f, (c) V2p, and (d) O1s for BVO-2 (red dash) and BVO-0 (black solid). (For interpretation of the references to colour in this figure legend, the reader is referred to the Web version of this article.)

positioned at 523.6 and 515.9 eV, related to the V2p_{1/2} and V2p_{3/2} states, confirming that vanadium is in the V⁵⁺ oxidation state [43]. Fig. 3b and c are consistent with the monoclinic scheelite phase of BiVO₄. The O1s peak in Fig. 3d, associated with metal oxides, appears at 529 eV. No shift was observed in the XPS signals from any of the three components, indicating that varying the pH did not alter the oxidation states of the elements in the deposited film.

The XRD patterns of BVO-0, BVO-1, BVO-1.5, and BVO-2 are presented in Fig. 4a. The XRD patterns of all samples show diffraction peaks at 2θ values of 28.6, 30.5, 34.5, 35.2, 39.5, 42.6, 46.0, 46.7, 47.3, 50.3, 53.3, 58.4, and 59.2°, corresponding to the (121), (040), (200), (002), (211), (150), (231), (240), (024), (202), (161), (321), and (123) planes, respectively. Thus, the diffraction patterns of all samples could be indexed to m-BiVO₄ (standard JCPDS card No. 14-0688). The absence of other peaks indicates the lack of crystalline impurities and demonstrates the presence of a single phase of BiVO₄. The intensity of the diffraction peaks of BVO-2 was slightly higher than that of BVO-0, which might be due to the higher crystallinity of the former. Thus, pH slightly alters the

crystallinity, but it does not influence the BiVO₄ crystal type [21,24]. Further, the diffraction peaks of ITO at 2θ of 30, 35, 50 and 59°, marked by diamonds, overlap with peaks of BiVO₄ and therefore could not be distinguished. Diffraction from BiVO₄ is stronger due to the high atomic number (high electron density) of Bi and because the BiVO₄ layer is substantially thicker than the ITO layer on the coated glass (~130 nm).

The XRD and XPS data confirm that the crystallinity and oxidation state of the elements remain unaltered as the pH change in the precursor drives changes in morphology of the deposited film. However, changes in chemical bonding were observed based on the Raman spectra presented in Fig. 4b. The peaks at 214, 327, 368, 651, and 827 cm⁻¹ are typical vibrational modes of m-BiVO₄. The peak at 214 cm⁻¹ is due to the external vibrational mode (rotation/translation) of BiVO₄. The peak reflections at 327 and 368 cm⁻¹ are assigned to the asymmetric (B_g) and symmetric (A_g) modes of the VO₄³⁻ tetrahedron, respectively. The broad hump located at 651 cm⁻¹ is assigned to the asymmetric V–O stretching vibration mode (B_g symmetry). However, the peak near 827 cm⁻¹ is

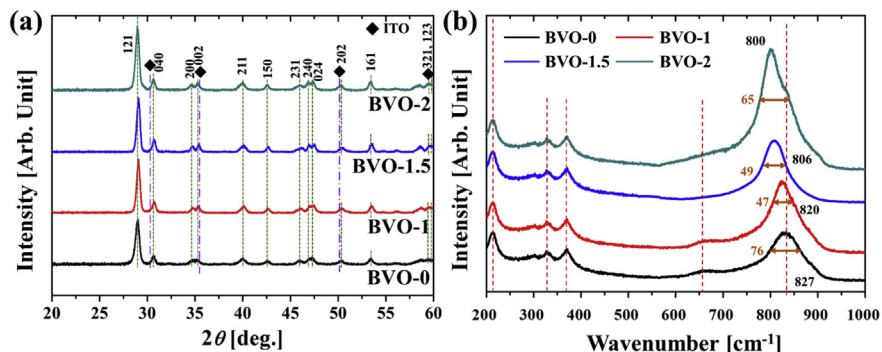


Fig. 4. (a) XRD patterns and (b) Raman spectra of all samples, as labeled.

due to the symmetric V–O stretching mode (A_g symmetry) and appears to be dominant in all cases. With increasing AH, the peak due to the VO_4 stretching mode at 827 cm^{-1} shifted to lower wavenumbers. This shift is inversely proportional to the length of the V–O bond according to the empirical formula given by Hardcastle et al. [44]. This implies that with increasing AH, the V–O bond length increases, suggesting structural distortion induced by modified electronic band structures [14,45]. Further, the full-width at half maximum (FWHM) first decreased and then increased with increasing addition of AH [46]. The increase in the pH from 0 to 4 changes the precursor solution from a strong acid to a weak acid; therefore, the FWHMs of BVO-1 (47 cm^{-1}) and BVO-1.5 (49 cm^{-1}) decrease compared to that of BVO-0 (65 cm^{-1}), which may be attributed to strong symmetric stretching due to agglomerated $BiVO_4$ particles. However, for BVO-2, when the pH is greater than 7, $BiVO_4$ nucleates more slowly, and hence, the large agglomeration of irregular particles causes weaker stretching vibration, thus increasing the FWHM (76 cm^{-1}) [47,48]. Zhang et al. [23] reported that the Raman band positions are highly sensitive to structural stability/distortion, whereas the FWHM is more sensitive to the crystallinity and other factors such as the particle size and defects. At higher synthesis $pH > 7$ of the precursor solution, the VO_4 tetrahedra are slightly distorted due to the increased bond length. However, the crystallinity is improved, and there are fewer defects than in the samples prepared at lower $pH (< 7)$. Our results are consistent with those reported by Zhang et al. [23].

The cross-sectional morphology and structural features of the BVO-2 sample were characterized by TEM, as shown in Fig. 5a and b. The high-resolution image in Fig. 5c shows the lattice fringes of the area marked in Fig. 5a. The fringes with interplanar spacings (d) of 0.312 and 0.292 nm correspond to the (121) and (040) planes of the monoclinic scheelite structure of $BiVO_4$ [49]. This agrees with the XRD results, further confirming that changing the pH of the precursor solution does not alter the crystal structure of $BiVO_4$, even though the particle size and surface morphology were significantly altered by the pH change, as demonstrated in Fig. 2. Elemental maps of the area enclosed in a white dashed square in Fig. 5a are shown in Fig. 5d, e, and f for Bi, V, and O, respectively.

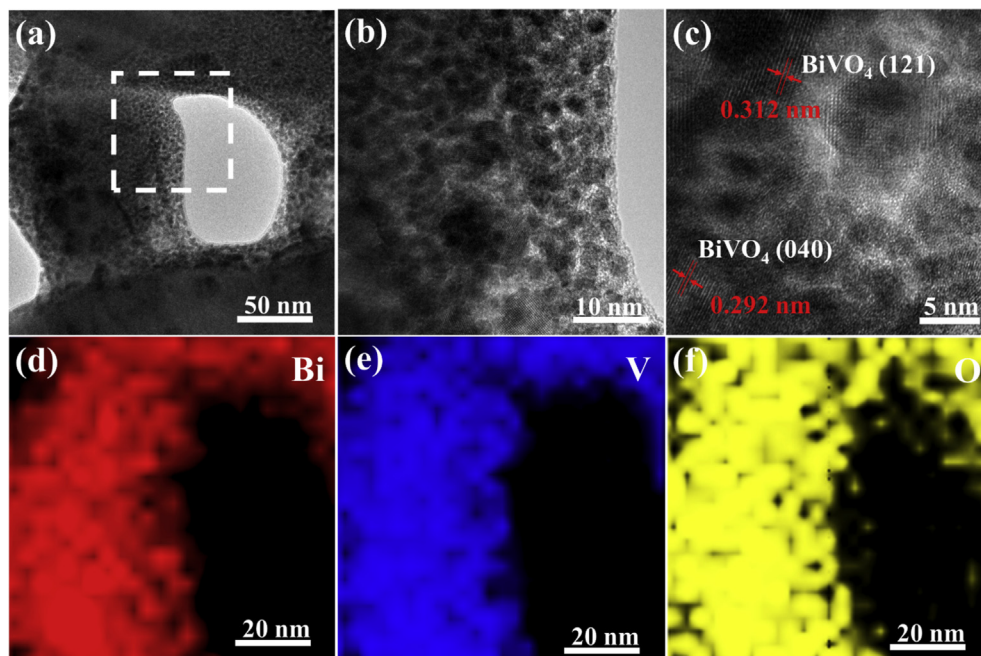


Fig. 5. TEM images of the BVO-2 sample (nanoferns) at various magnifications (a–c), Elemental mapping of the BVO-2 sample by EDX for (d) Bi, (e) V, and (f) O.

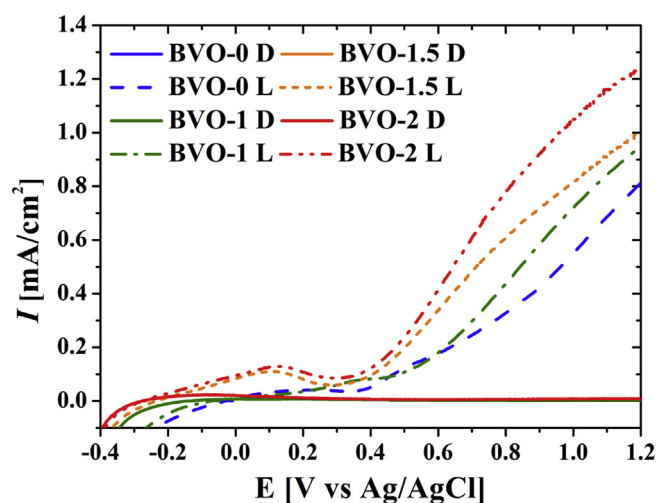


Fig. 6. Current–voltage (I – V) curves for the $BiVO_4$ films deposited from precursors with varying amounts of AH (0, 1, 1.5 and 2 ml). D and L indicate measurements in the dark and under illumination, respectively.

3.2. Photoelectrochemical properties

Fig. 6 shows PCD values of the single absorber photoanode $BiVO_4$ samples prepared from precursors of varying pH. The PCD of the BVO-0 film was 0.82 mA cm^{-2} at 1.2 V vs. Ag/AgCl, compared to PCD values of 0.95, 1.0, and 1.23 mA cm^{-2} for BVO-1, BVO-1.5, and BVO-2, respectively. Three major processes, i.e., photoexcitation, surface/bulk recombination, and charge separation, are involved in the photoreaction over the photocatalytic material under consideration. During the PEC process at the photoanode, photoexcited electrons are transferred towards ITO, and the holes react at the electrode/electrolyte interface. Modifying the morphology of the $BiVO_4$ pillars to the fern-like structure improves the photocurrent and decreases bulk recombination, as is evident from the results presented in Fig. 6. BVO-0 presented the lowest photocurrent,

whereas the photoanodes deposited with increasing pH showed increased photocurrent density, where the SEM images indicate that the fern-like structure is made up of much finer (thinner) structures than the BVO-0 pillars. Thus, the fern-like structure exposes more BiVO_4 particle surface area to the electrolyte, and consequently, the PEC performance improves. Additionally, the charge transfer impedance also decreased for BVO-2 due to the better optical penetration depth. We also investigated the stability of each photoanode at 0.6 V, as shown in Fig. S2.

Fig. 7 shows the Bode phase plots as determined from EIS measurements performed under back illumination. The frequency range for the analysis was 100 kHz to 100 mHz for all the samples. Fig. 7a shows the Bode plot for BVO-0 and BVO-2 under illumination. BVO-0 and BVO-2 showed identical electrochemical responses under dark conditions. However, under illumination, the samples displayed significantly different responses. Notably, the XRD patterns of both samples were similar, suggesting that the integrity of BiVO_4 was well preserved. Thus, the change in the PEC response for BVO-2 could be attributed to the engineered morphology, which resulted in spatial charge separation at the facets exposed to the electrolyte, thereby improving the photocatalytic reactivity [50]. The shift in the characteristic frequency for BVO-2 case relative to that of BVO-0 is presented in Fig. 7b with a magnified view, along with the Randle equivalent circuit and the corresponding circuit parameters (Fig. 7c) obtained by fitting the raw data.

Furthermore, Fig. 7b reveals that both cases show two peaks. The medium-frequency peak in the Bode phase plot corresponds to the depletion layer [51], whereas the low-frequency peak arises from the impedance of the Helmholtz layer. The depletion layer suggests electron transfer, whereas the Helmholtz layer corresponds to the capacitance developed at the semiconductor/electrolyte interface to counterbalance the disequilibrium occurring due to the redox potential. The Bode plot in Fig. 7b for BVO-0 does not show a significant peak at a lower frequency, unlike the plot for BVO-2, suggesting that the depletion layer may be thick, which limits charge transfer. However, the clear peaks for BVO-2 could be attributed to the fern-like morphology of BiVO_4 (see SEM images in Fig. 2).

The charge transport time factor (τ_n) for electron recombination was determined from the characteristic frequency (f_m), which corresponds to the peak phase angle in the Bode plot. The charge transport time factor was calculated using the following equation [52]:

$$\tau_n = \frac{1}{2\pi f_m} \quad (1)$$

With the addition of AH to BiVO_4 , the characteristic frequency or the frequency corresponding to the peak phase angle in the Bode plot increased, as indicated by the blue and red vertical lines in Fig. 7a. This shift in the characteristic frequency, as mentioned earlier, is attributed to the change in the morphology of BiVO_4 from pillar to fern-like, consequently yielding a lower charge transfer time factor. The charge transport time factor (Fig. 7c) for electron–hole recombination decreased from 3.53 to 1.93 ms when the amount of AH added was increased from 0 to 2 mL. Although the charge transport time factor decreased, which indicates faster recombination, the PCD of BVO-2 was larger than that of BVO-0, which may be due to the lower solution impedance, as well as the lower charge transfer impedance of BVO-2. The lower impedance, in this case, is enough to maintain the larger electron flow from the semiconductor layer, and thus the photocatalytic kinetics become much faster, as evidenced by the PCD presented in Fig. 6. The impedance values for both cases are presented in Fig. 7c. Here, R_s is the solution impedance, R_{dl} is the charge transfer impedance associated with the bulk material (interior of the photoanode material), and R_H is associated with charge transfer at the photoanode/electrolyte interface. Furthermore, Q_H and Q_{dl} are the capacitances associated with the Helmholtz double layer and the depletion layer in the semiconductor, respectively. The fitted Nyquist data for samples BVO-0 and BVO-2 are shown in Fig. S3. The values of R_s and R_H are lower for BVO-2 than those for BVO-0. These results suggest that compared to BVO-0, BVO-2 has a larger exposed area for electrolyte diffusion and shorter charge transfer pathways in the bulk (interior) region of the electrode due to its fern-like morphology. Furthermore, Q_{dl} and R_{dl} for BVO-2 were observed to be larger than those for BVO-0, which ensures that the electron–hole separation at the electrode–electrolyte interface is consistent with the PCD demonstrated in Fig. 6.

A possible mechanism for photocatalytic splitting water is illustrated in Fig. 8. The water splitting process is complex, involving steps such as photon absorption that depend on the material, its morphology, electronic structure, exciton separation, catalytic efficiency, carrier diffusion, and transport. However, to simplify the photocatalytic/electrocatalytic steps for water splitting during illumination, we present here a schematic illustration of the

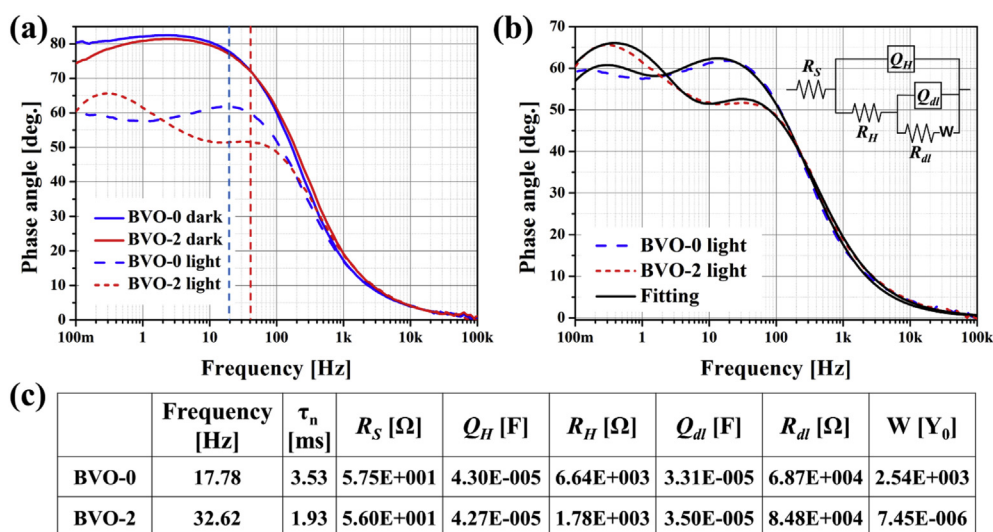


Fig. 7. (a) Bode phase plots of BVO-0 and BVO-2, (b) magnified view of Bode plots, and (c) parameters deduced at characteristic frequencies for BVO-0 and BVO-2.

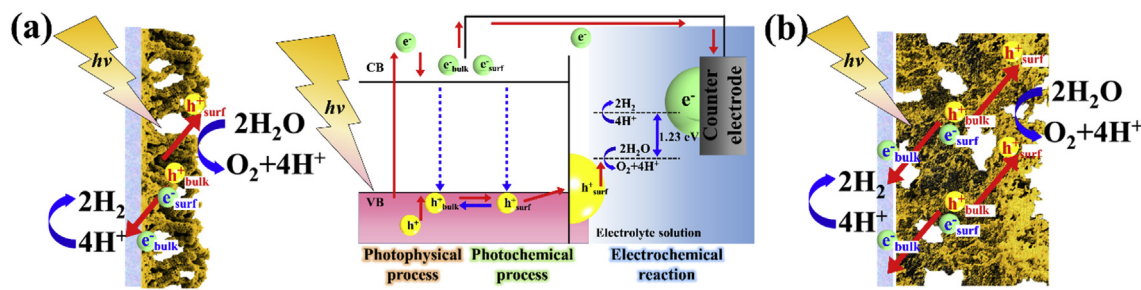


Fig. 8. Schematic illustration demonstrating the PEC process for water splitting at the photoanode (a) BVO-0 and (b) BVO-2 under illumination.

mechanism. When the photons are incident on the photoanode, a photophysical process generates an electron–hole pair. This process is highly dependent on the morphology of the photoanode material for higher photon absorption. The PEC mechanism depicted in Fig. 8a occurs for BVO-0 when the morphology is pillar-like with slightly thick pillars that limit the available electrochemical reaction sites for reaction of holes with water. In contrast, the fern-like morphology of BVO-2 (see Fig. 8b) provides more reactive sites and shorter transport distances for holes while maintaining a continuous transport pathway for electrons to reach the external circuit thanks to its branched structure. Photoexcited electrons diffuse toward ITO, while holes move toward the electrode–electrolyte interface, and the resulting electron–hole separation forms a depletion layer and a Helmholtz layer at the surface. However, along with separation, migration of the electrons is also significant. Here, the fern-like structure with lower R_S and R_H enables a fast kinetic redox reaction. Lastly, the electrochemical process at the surface of BiVO_4 (where the holes/electrolyte are involved in the redox reaction) results in O_2 evolution. Thus, based on the morphological analysis of BiVO_4 deposited by electrospray and PCD analysis, the present sample is highly efficient for all three processes involved in water splitting.

4. Conclusions

By adjusting the pH of the BiVO_4 precursor solution used in ESD by adding AH, the morphology of BiVO_4 nanopillars was transformed from pillars into a nanofern structure with a higher overall surface area. The thin, wide ferns facilitated faster water oxidation owing to the increased interfacial area between the BiVO_4 electrode and electrolyte. Thus, the rate of surface reaction of holes with water/electrolyte increased, and the PEC performance of the BiVO_4 system improved, as confirmed by comparing the photocurrent density of the films fabricated from precursors of varying pH. SEM images illustrated the change in morphology and the increase in surface area, while Bode phase plots from EIS were used to explain the improvement in the film performance with increasing pH.

Acknowledgment

This research was supported by the Technology Development Program to Solve Climate Changes of the National Research Foundation (NRF) funded by the Ministry of Science, ICT & Future Planning (NRF-2016M1A2A2936760) and NRF-2017R1A2B4005639.

Appendix A. Supplementary data

Supplementary data related to this article can be found at <https://doi.org/10.1016/j.jallcom.2018.07.167>.

References

- [1] A. Fujishima, Electrochemical photolysis of water at a semiconductor electrode, *Nature* 238 (1972) 37–38.
- [2] P. Lianos, Review of recent trends in photoelectrocatalytic conversion of solar energy to electricity and hydrogen, *Appl. Catal., B* 210 (2017) 235–254.
- [3] Y.W. Phuan, W.-J. Ong, M.N. Chong, J.D. Ocon, Prospects of electrochemically synthesized hematite photoanodes for photoelectrochemical water splitting: a review, *J. Photochem. Photobiol., C* 33 (2017) 54–82.
- [4] A. Wolcott, W.A. Smith, T.R. Kuykendall, Y. Zhao, J.Z. Zhang, Photoelectrochemical water splitting using dense and aligned TiO_2 nanorod arrays, *Small* 5 (2009) 104–111.
- [5] S. Hejazi, N.T. Nguyen, A. Mazare, P. Schmuki, Aminated TiO_2 nanotubes as a photoelectrochemical water splitting photoanode, *Catal. Today* 281 (2017) 189–197.
- [6] D. Chen, Z. Liu, M. Zhou, P. Wu, J. Wei, Enhanced photoelectrochemical water splitting performance of $\alpha\text{-Fe}_2\text{O}_3$ nanostructures modified with Sb_2S_3 and cobalt phosphate, *J. Alloys Compd.* 742 (2018) 918–927.
- [7] Q. Liu, C. Chen, G. Yuan, X. Huang, X. Lü, Y. Cao, Y. Li, A. Hu, X. Lu, P. Zhu, Morphology-controlled $\alpha\text{-Fe}_2\text{O}_3$ nanostructures on FTO substrates for photoelectrochemical water oxidation, *J. Alloys Compd.* 715 (2017) 230–236.
- [8] S. Mohite, V. Ganbavle, K. Rajpure, Solar photoelectrocatalytic activities of rhodamine-B using sprayed WO_3 photoelectrode, *J. Alloys Compd.* 655 (2016) 106–113.
- [9] J.C. Hill, K.-S. Choi, Effect of electrolytes on the selectivity and stability of n-type WO_3 photoelectrodes for use in solar water oxidation, *J. Phys. Chem. C* 116 (2012) 7612–7620.
- [10] H. Yoon, M.G. Mali, J.Y. Choi, M.-W. Kim, S.K. Choi, H. Park, S.S. Al-Deyab, M.T. Swihart, A.L. Yarin, S.S. Yoon, Nanotextured pillars of electrosprayed bismuth vanadate for efficient photoelectrochemical water splitting, *Langmuir* 31 (2015) 3727–3737.
- [11] X. Wang, K.-H. Ye, X. Yu, J. Zhu, Y. Zhu, Y. Zhang, Polyaniline as a new type of hole-transporting material to significantly increase the solar water splitting performance of BiVO_4 photoanodes, *J. Power Sources* 391 (2018) 34–40.
- [12] G. Wang, Y. Yang, Y. Ling, H. Wang, X. Lu, Y.-C. Pu, J.Z. Zhang, Y. Tong, Y. Li, An electrochemical method to enhance the performance of metal oxides for photoelectrochemical water oxidation, *J. Mater. Chem. A* 4 (2016) 2849–2855.
- [13] B. Pattengale, J. Huang, The effect of Mo doping on the charge separation dynamics and photocurrent performance of BiVO_4 photoanodes, *Phys. Chem. Chem. Phys.* 18 (2016) 32820–32825.
- [14] V. Merupo, S. Velumani, G. Oza, M. Makowska-Janusik, A. Kassiba, Structural, electronic and optical features of molybdenum-doped bismuth vanadium oxide, *Mater. Sci. Semicond. Process.* 31 (2015) 618–623.
- [15] S. Balachandran, N. Prakash, K. Thirumalai, M. Muruganandham, M. Sillanpää, M. Swaminathan, Facile construction of heterostructured $\text{BiVO}_4\text{-ZnO}$ and its dual application of greater solar photocatalytic activity and self-cleaning property, *Ind. Eng. Chem. Res.* 53 (2014) 8346–8356.
- [16] X. Zhang, B. Zhang, K. Cao, J. Brillet, J. Chen, M. Wang, Y. Shen, A perovskite solar cell- $\text{TiO}_2\text{/BiVO}_4$ photoelectrochemical system for direct solar water splitting, *J. Mater. Chem. A* 3 (2015) 21630–21636, <https://doi.org/10.1039/C5TA05838D>.
- [17] M.G. Mali, H. Yoon, M.-W. Kim, M.T. Swihart, S.S. Al-Deyab, S.S. Yoon, Electrosprayed heterojunction $\text{WO}_3\text{/BiVO}_4$ films with nanotextured pillar structure for enhanced photoelectrochemical water splitting, *Appl. Phys. Lett.* 106 (2015) 151603.
- [18] N. Micali, F. Neri, P.M. Ossi, S. Trusso, Light scattering enhancement in nanostructured silver film composites, *J. Phys. Chem. C* 117 (2013) 3497–3502.
- [19] H. Jung, S.Y. Chae, H. Kim, B.K. Min, Y.J. Hwang, Electrospun Mo-doped BiVO_4 photoanode on a transparent conductive substrate for solar water oxidation, *Catal. Commun.* 75 (2016) 18–22.
- [20] C. Liu, J. Li, Y. Li, W. Li, Y. Yang, Q. Chen, Epitaxial growth of Bi_2S_3 nanowires on BiVO_4 nanostructures for enhancing photoelectrochemical performance, *RSC Adv.* 5 (2015) 71692–71698.
- [21] Y. Lu, H. Shang, F. Shi, C. Chao, X. Zhang, B. Zhang, Preparation and efficient visible light-induced photocatalytic activity of m- BiVO_4 with different

- morphologies, *J. Phys. Chem. Solids* 85 (2015) 44–50.
- [22] M. Wu, Q. Jing, X. Feng, L. Chen, BiVO₄ microstructures with various morphologies: synthesis and characterization, *Appl. Surf. Sci.* 427 (2018) 525–532.
- [23] A. Zhang, J. Zhang, N. Cui, X. Tie, Y. An, L. Li, Effects of pH on hydrothermal synthesis and characterization of visible-light-driven BiVO₄ photocatalyst, *J. Mol. Catal. A Chem.* 304 (2009) 28–32.
- [24] F. Li, C. Yang, Q. Li, W. Cao, T. Li, The pH-controlled morphology transition of BiVO₄ photocatalysts from microparticles to hollow microspheres, *Mater. Lett.* 145 (2015) 52–55.
- [25] S. Dong, J. Feng, Y. Li, L. Hu, M. Liu, Y. Wang, Y. Pi, J. Sun, J. Sun, Shape-controlled synthesis of BiVO₄ hierarchical structures with unique natural-sunlight-driven photocatalytic activity, *Appl. Catal., B* 152 (2014) 413–424.
- [26] L. Chen, J. Wang, D. Meng, X. Wu, Y. Wang, E. Zhong, The pH-controlled {040} facets orientation of BiVO₄ photocatalysts with different morphologies for enhanced visible light photocatalytic performance, *Mater. Lett.* 162 (2016) 150–153.
- [27] M.-W. Kim, K. Kim, T.Y. Ohm, B. Joshi, E. Samuel, M.T. Swihart, H. Yoon, H. Park, S.S. Yoon, Mo-doped BiVO₄ nanotextured pillars as efficient photoanodes for solar water splitting, *J. Alloys Compd.* 726 (2017) 1138–1146.
- [28] J. Tang, A. Gomez, Controlled mesoporous film formation from the deposition of electrosprayed nanoparticles, *Aerosol Sci. Technol.* 51 (2017) 755–765.
- [29] H. Ueda, K. Takeuchi, A. Kikuchi, Effect of the nozzle tip's geometrical shape on electrospray deposition of organic thin films, *Jpn. J. Appl. Phys.* 56 (2017), 04CL05.
- [30] J. He, Y. Sun, M. Wang, Z. Geng, X. Wu, L. Wang, H. Chen, K. Huang, S. Feng, Direct growth of NiCo₂O₄ nanostructure on conductive substrate by electrospray technique for oxygen evolution reaction, *J. Alloys Compd.* 752 (2018) 389–394.
- [31] K.-W. Nam, K.-B. Kim, Manganese oxide film electrodes prepared by electrostatic spray deposition for electrochemical capacitors, *J. Electrochem. Soc.* 153 (2006) A81–A88.
- [32] M.-W. Kim, B. Joshi, H. Yoon, T.Y. Ohm, K. Kim, S.S. Al-Deyab, S.S. Yoon, Electrosprayed copper hexaoxodivanadate (CuV₂O₆) and pyrovanadate (Cu₂V₂O₇) photoanodes for efficient solar water splitting, *J. Alloys Compd.* 708 (2017) 444–450.
- [33] X. Gao, Z. Wang, F. Fu, W. Li, Effects of pH on the hierarchical structures and photocatalytic performance of Cu-doped BiVO₄ prepared via the hydrothermal method, *Mater. Sci. Semicond. Process.* 35 (2015) 197–206.
- [34] M. Nikolaou, T. Krasia-Christoforou, Electrohydrodynamic methods for the development of pulmonary drug delivery systems, *Eur. J. Pharm. Sci.* 113 (2017) 29–40.
- [35] Y. Zhang, H. Gong, Y. Zhang, K. Liu, H. Cao, H. Yan, J. Zhu, The controllable synthesis of octadecahedral BiVO₄ with exposed {111} facets, *Eur. J. Inorg. Chem.* 2017 (2017) 2990–2997.
- [36] L. Zhang, W. Wang, L. Zhou, H. Xu, Bi₂WO₆ nano- and microstructures: shape control and associated visible-light-driven photocatalytic activities, *Small* 3 (2007) 1618–1625.
- [37] X.-H. Guo, S.-H. Yu, Controlled mineralization of barium carbonate mesocrystals in a mixed solvent and at the air/solution interface using a double hydrophilic block copolymer as a crystal modifier, *Cryst. Growth Des.* 7 (2007) 354–359.
- [38] Y. Ma, H. Jiang, X. Zhang, J. Xing, Y. Guan, Synthesis of hierarchical m-BiVO₄ particles via hydro-solvothermal method and their photocatalytic properties, *Ceram. Int.* 40 (2014) 16485–16493.
- [39] M.L. Brongersma, Y. Cui, S. Fan, Light management for photovoltaics using high-index nanostructures, *Nat. Mater.* 13 (2014) 451.
- [40] T.W. Kim, Y. Ping, G.A. Galli, K.-S. Choi, Simultaneous enhancements in photon absorption and charge transport of bismuth vanadate photoanodes for solar water splitting, *Nat. Commun.* 6 (2015) 8769.
- [41] K.P.S. Parmar, H.J. Kang, A. Bist, P. Dua, J.S. Jang, J.S. Lee, Photocatalytic and photoelectrochemical water oxidation over metal-doped monoclinic BiVO₄ photoanodes, *ChemSusChem* 5 (2012) 1926–1934.
- [42] S.K. Pilli, T.E. Furtak, L.D. Brown, T.G. Deutsch, J.A. Turner, A.M. Herring, Cobalt-phosphate (Co-Pi) catalyst modified Mo-doped BiVO₄ photoelectrodes for solar water oxidation, *Energy Environ. Sci.* 4 (2011) 5028–5034.
- [43] M. Zalfani, B. van der Schueren, Z.-Y. Hu, J.C. Rooke, R. Bourguiga, M. Wu, Y. Li, G. Van Tendeloo, B.-L. Su, Novel 3DOM BiVO₄/TiO₂ nanocomposites for highly enhanced photocatalytic activity, *J. Mater. Chem. A* 3 (2015) 21244–21256.
- [44] F.D. Hardcastle, I.E. Wachs, Determination of vanadium-oxygen bond distances and bond orders by Raman spectroscopy, *J. Phys. Chem.* 95 (1991) 5031–5041.
- [45] J. Yu, A. Kudo, Effects of structural variation on the photocatalytic performance of hydrothermally synthesized BiVO₄, *Adv. Funct. Mater.* 16 (2006) 2163–2169.
- [46] M. Gotic, S. Musić, M. Ivanda, M. Šoufek, S. Popović, Synthesis and characterisation of bismuth (III) vanadate, *J. Mol. Struct.* 744 (2005) 535–540.
- [47] L. Dong, S. Guo, S. Zhu, D. Xu, L. Zhang, M. Huo, X. Yang, Sunlight responsive BiVO₄ photocatalyst: effects of pH on L-cysteine-assisted hydrothermal treatment and enhanced degradation of ofloxacin, *Catal. Commun.* 16 (2011) 250–254.
- [48] S. Phiankoh, R. Munprom, Effect of pH on crystal structure and morphology of hydrothermally-synthesized BiVO₄, *Mater. Today* 5 (2018) 9447–9452.
- [49] M. Huang, J. Bian, W. Xiong, C. Huang, R. Zhang, Low-dimensional Mo: BiVO₄ photoanodes for enhanced photoelectrochemical activity, *J. Mater. Chem. A* 6 (2018) 3602–3609.
- [50] R. Li, Latest progress in hydrogen production from solar water splitting via photocatalysis, photoelectrochemical, and photovoltaic-photoelectrochemical solutions, *Chin. J. Catal.* 38 (2017) 5–12.
- [51] T. Lopes, L. Andrade, F. Le Formal, M. Gratzel, K. Sivula, A. Mendes, Hematite photoelectrodes for water splitting: evaluation of the role of film thickness by impedance spectroscopy, *Phys. Chem. Chem. Phys.* 16 (2014) 16515–16523.
- [52] J.A. Seabold, K. Zhu, N.R. Neale, Efficient solar photoelectrolysis by nanoporous Mo: BiVO₄ through controlled electron transport, *Phys. Chem. Chem. Phys.* 16 (2014) 1121–1131.